Available online at www.sciencedirect.com
SCIENCE DIRECT
Tectonophysics 420 (2006) 205–221
TECTONOPHYSICS
www.elsevier.com/locate/tecto

Moho depth variation beneath southwestern Japan revealed from the velocity structure based on receiver function inversion

Katsuhiko Shiomi [a,*], Kazushige Obara [a,1], Haruo Sato [b,2]

[a] National Research Institute for Earth Science and Disaster Prevention 3-1, Tennodai, Tsukuba-shi, Ibaraki-ken 305-0006, Japan
[b] Graduate School of Science, Tohoku University 6-3, Aramaki Aoba, Aoba-ku, Sendai, Miyagi 980-8578, Japan

Received 29 January 2005; received in revised form 24 October 2005; accepted 4 January 2006
Available online 29 March 2006

Abstract

The Philippine Sea plate is subducting under the Eurasian plate beneath the Chugoku-Shikoku region, southwestern Japan. We have constructed depth contours for the continental and oceanic Mohos derived from the velocity structure based on receiver function inversion. Receiver functions were calculated using teleseismic waveforms recorded by the high-density seismograph network in southwestern Japan. In order to determine crustal velocity structure, we first improved the linearized time-domain receiver function inversion method. The continental Moho is relatively shallow (~30 km) at the coastline of the Sea of Japan and at the Seto Inland Sea, and becomes deeper–greater than 40 km–around 35°N and 133.8°E. Near the Seto Inland Sea, a low-velocity layer of thickness 10 km lies under the continental Moho. This low-velocity layer corresponds to the subducting oceanic crust of the Philippine Sea plate. The oceanic Moho continues to descend from south to northwest and exhibits complicated ridge and valley features. The oceanic Moho runs around 25 km beneath the Pacific coast and 45 km beneath the Seto Inland Sea, and it extends to at least to 34.5°N. The depth variation of the Moho discontinuities is in good qualitative agreement with the concept of isostasy. From the configurations of both the continental and oceanic Mohos, we demonstrate that the continental lower crust and the subducting oceanic crust overlap beneath the southern and central part of Shikoku and that a mantle wedge may exist beneath the western and eastern part of Shikoku. The southern edge of the overlapping region coincides with the downdip limit of the slip area of a megathrust earthquake.

Keywords: Continental Moho; Oceanic Moho; Philippine Sea plate; Southwestern Japan; Receiver function

1. Introduction

The seismic wave velocity changes significantly at the boundary between the crust and the uppermost mantle. This velocity gap is referred to as the Mohorovičić (Moho) discontinuity. Along a subduction zone, the configurations of the Moho within the continental plate and the oceanic slab provide important information for estimating the downdip limit of megathrust earthquakes rupture (e.g., Oleskevich et al., 1999). In the Chugoku-Shikoku region, southwestern Japan, the Philippine Sea plate (PHS) is subducting beneath the Eurasian plate (EUR) from the Nankai Trough. The subduction of the PHS has caused large earthquakes in the Nankai region with magnitudes (M) of around 8 (e.g., Ando, 1975). Both the continental

* Corresponding author. Fax: +81 29 860 2317.
E-mail addresses: shiomi@bosai.go.jp (K. Shiomi), obara@bosai.go.jp (K. Obara), sato@zisin.geophys.tohoku.ac.jp (H. Sato).
[1] Fax: +81 29 860 2317.
[2] Fax: +81 22 217 6783.

0040-1951/$ - see front matter © 2006 Elsevier B.V. All rights reserved.
doi:10.1016/j.tecto.2006.01.017

Moho of the EUR and oceanic Moho of the PHS exist in this region. In order to clarify seismotectonics in southwestern Japan, knowledge of the detailed structure of the crust and uppermost mantle, especially the configurations of both the Moho and slab, is very important.

Fig. 1 is an index map of the Chugoku-Shikoku region, southwestern Japan. For this region, the two-dimensional P-wave velocities and the depth variations of the Moho and other velocity discontinuities were constructed based on a series of reflection and/or refraction surveys (e.g., Yoshii et al., 1974; Ito et al., 1982; Kodaira et al., 2002; Kurashimo et al., 2002). Ryoki (1999) compiled the results of artificial explosion surveys and constructed depth contours for the Moho. According to his result, the Moho is located at a depth of 30 km beneath the Pacific (southern) and Sea of Japan (northern) coasts and attains a depth of 38 km beneath the central part of Shikoku. However, the resolution of his result is rather poor because the contour map was constructed by the interpolation of only a few two-dimensional profiles. Zhao et al. (1992) estimated the depth variation of the Moho and the Conrad discontinuity beneath Japan based on travel time inversion analysis. Their result, in general, exhibits the same tendency as the depth contour by Ryoki (1999), with the exception that they located the deepest point of the Moho at the western part of Shikoku at a depth of 38 km. However, their result is not very reliable because the number of rays that refract at the Moho beneath the Chugoku region are too few due to the sparseness of the seismograph stations at the time. In this region, travel time tomography studies on velocity structure have been carried out by Hirahara (1981), Zhao et al. (2002), Honda and Nakanishi (2003) and Matsubara et al. (2003). They attempted to reveal the inhomogeneities of the velocity structure and imaged the subducting PHS. The tomography technique, however, is inherently inefficient at detecting a sharp velocity change like that which occurs at the Moho. Moreover, the inhomogeneous distribution of local earthquakes and grid intervals greatly affected the resolution of their results. From another point of view, Ohkura (2000) claimed that the continental lower crust and subducting oceanic crust overlap beneath almost the entire region of Shikoku Island; this was based on the analyses of the later phases following the initial P- and S-waves. His result indicates that only the oceanic Moho exists beneath most of the Shikoku region and a sudden change in crustal thickness should be expected at the boundary of a region where the continental crust directly overlies (i.e., is attached to) the oceanic crust. Neither of the previous studies presented such a sudden change in the crustal thickness, owing to the insufficient spatial resolution of the data.

Recently, receiver functions have been frequently applied to image the Moho, subducting slab and other velocity discontinuities beneath seismograph stations. A receiver function is defined by the removal of a source-time function from the radial and transverse component

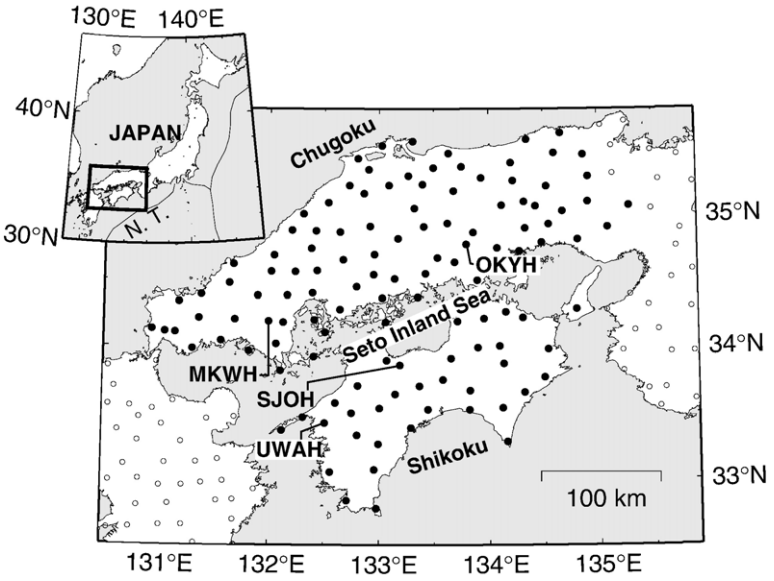

Fig. 1. Index map of the Chugoku-Shikoku region, where "N.T." refers to the "Nankai Trough". Circles indicate the distribution of the Hi-net seismograph stations. Solid circles denote the stations used in this study.

trace by using a deconvolution technique. This method uses only the relative travel time delay between the P-to-S converted phases and the direct P-wave. Some researchers calculate a depth-converted receiver function by using a suitable velocity model to investigate the depth variation of the continental Moho (e.g., Zhu, 2000; Galvé et al., 2002) and/or the subducting slab (e.g., Li et al., 2000; Yuan et al., 2000; Ferris et al., 2003; Shiomi et al., 2004). Zhu and Kanamori (2000) proposed a simple stacking method for multiple phases between the ground surface and the Moho, and they used a grid search technique to determine both the thickness and Poisson's ratio of the crust in southern California. Velocity inversion methods that employed receiver functions were also used to evaluate crustal structure and thickness (e.g., Soda et al., 2001; Zorin et al., 2002; Chang et al., 2004).

The National Research Institute for Earth Science and Disaster Prevention established a high-sensitivity seismograph network (Hi-net) across Japan; the average station interval of this network was 20 km (Okada et al., 2004). The high density of Hi-net has enabled us to investigate the underground structure beneath Japan in detail. Shiomi et al. (2004) estimated the receiver functions by using teleseismic waveform data recorded at the Hi-net stations. They constructed a detailed configuration of the oceanic Moho of the PHS subducting beneath Shikoku from south to northwest with a low dip angle. Although they observed a velocity discontinuity corresponding to the continental Moho in the northern part of the Chugoku region, it is not evident in the southern part.

In this paper, we invert receiver functions calculated from the teleseismic waveforms recorded by Hi-net in order to obtain a seismic velocity structure. We determine the depth of clear discontinuities from the estimated velocity models and map the Moho depths at the P-to-S conversion points. Based on vertical cross sections, we classify all the conversion points as continental or oceanic Moho. By interpolating the result, we draw separate depth contours for the continental and the oceanic Moho beneath the Chugoku-Shikoku region. Finally, we discuss the characteristics of the Moho depth variation and the inhomogeneity of the crustal structure.

2. Receiver function and velocity inversion

Receiver functions emphasize the P-to-S converted phases from teleseismic waves through a deconvolution of the radial and transverse component traces by the vertical one. Travel time delays and amplitudes of these converted phases provide important information regarding underground velocity structures. In the frequency domain, the receiver function is defined as

$$H_R(f) = R(f)/Z(f), \quad H_T(f) = T(f)/Z(f), \tag{1}$$

where $R(f)$, $T(f)$ and $Z(f)$ are the radial, transverse and vertical component spectra, respectively. Using the inverse Fourier transform of $H_R(f)$ and $H_T(f)$, we obtain the time-domain receiver functions $h_R(t)$ and $h_T(t)$. Various methods have been proposed for the estimation of a receiver function. In this paper, we employ receiver functions estimated by using the multivariate autoregressive (MAR) model method (Shiomi et al., 2004). This algorithm enables one to avoid both the arbitrariness of the parameter selection, for example, the water-level (e.g., Helmberger and Wiggins, 1971), and the instability of the deconvolution process.

As mentioned above, the lapse time of the receiver function is generally converted into depth by using an appropriate local velocity model to image the variation in the velocity discontinuities. However, the reliability of the image depends on the accuracy of the local velocity models. The simple stacking method proposed by Zhu and Kanamori (2000) requires only an average crustal P-wave velocity as an input parameter. However, since two types of Moho lie beneath the southwestern part of Japan, it is difficult to analyze the continental and/or oceanic Moho depth separately. Hence, in this paper, we invert for seismic velocity structure from receiver functions and then identify a layer interface exhibiting a velocity change as a Moho.

2.1. Velocity inversion method

A one-dimensional seismic wave velocity structure can be constructed by inverting receiver functions. Ammon et al. (1990) proposed a linearized inversion method in which the amplitude information of the receiver functions is also included. In this method, the Poisson's ratio of each layer is fixed and a smoothing parameter is used to reduce the roughness of the inversion model. Several methods have been proposed to suppress the nonuniqueness of the inversion result. Since the dispersion curves of the surface waves provide information on the large-scale S-wave structure, Du and Foulger (1999) proposed an inversion method that simultaneously solves for both the receiver functions and a dispersion curve. Soda et al. (2001) later proposed another improved method in which an inversion model is constrained to an initial model derived from travel time tomography analysis. Although, in practise, the Poisson's ratio varies with region and/or depth (e.g., Kamiya and Kobayashi, 2000; Zhao et al., 2002), in many

cases, only S-wave velocity models have been estimated from the receiver function inversions. This is primarily because the receiver functions are mainly controlled by S-wave velocity since they are constructed by using the time delay between the P and P-to-S converted phases. Thus, radial receiver functions hold little information about the P-wave velocity. Fig. 2 shows the effect of P-wave velocity on a receiver function. We employed two model structures having different Poisson's ratios (left panel of Fig. 2). For a wavelet with an incidence angle of 28°, we calculated the receiver functions by using the propagator matrix method (Kennett and Kerry, 1979). Although the S-wave velocity models are the same, the receiver functions shown in the right panel of Fig. 2 are clearly different. This discrepancy is caused by the difference in the Poisson's ratio. Because the assumption of a constant Poisson's ratio may result in an inappropriate velocity model, the Poisson's ratio or the P-wave velocity should not be fixed for the receiver function inversion process.

In order to determine shallow structures such as the crust and uppermost mantle and to reduce the nonuniqueness of the receiver function inversion, we propose an improved receiver function inversion technique. In order to estimate velocity structure from receiver functions, Ammon et al. (1990) introduced a linearized inversion method defined as

$$(\mathbf{D}_S)_j \cdot \vec{s} \approx (\vec{r}_S)_j + (\mathbf{D}_S)_j \cdot \vec{s_0}, \tag{2}$$

where $\vec{s}$ and $\vec{s_0}$ denote an L layer one-dimensional S-wave velocity model and an initial model, respectively. The parameter j indicates the index of the receiver functions and $(\vec{r}_S)_j$ represents the N-dimensional residual vector for the jth receiver function. Each receiver function is sampled with a time interval Δt and consists of N data points. The $N \times L$ matrix $(\mathbf{D}_S)_j$ represents partial derivatives of the structural model response for the incidence angle of the jth receiver function. The thickness of each layer of the model is fixed during iterations.

In the frequency domain, we can rewrite Eq. (1) as

$$\begin{aligned} H_R(f) &= R(f)/Z(f) = R(f)Z(f)^*/Z(f)Z(f)^*, \\ H_T(f) &= T(f)/Z(f) = T(f)Z(f)^*/Z(f)Z(f)^*, \end{aligned} \tag{3}$$

where the asterisk means complex conjugation. These equations mean that a receiver function is defined by the ratio of the cross spectrum between the horizontal and vertical components to the power spectrum of the vertical component. This means that a receiver function is considered to be a filtered cross-correlation function without a phase change. The accuracy of a correlation function estimated from finite data generally decreases with an increase in lag time. The same principle can be applied to a receiver function. The accuracy of a receiver function also decreases with increasing lapse time. In addition, a receiver function may be contaminated by reverberation phases between uncertain depths and diffraction phases at later lag times. In order to avoid these contaminations, we introduce an $N \times N$ matrix $\mathbf{W}$ that emphasizes the data at an earlier lag time:

$$\mathbf{W} = \begin{bmatrix} w_1 & 0 & 0 & \cdots \\ 0 & w_2 & 0 & \cdots \\ 0 & 0 & w_3 & \cdots \\ \vdots & \vdots & \vdots & \ddots \end{bmatrix}, \tag{4}$$

where $w_i (i = 1, 2, \cdots, N)$ is a discrete time-domain weighting function with a time interval Δt. Fig. 3(a) shows the weighting function w used in this study. The horizontal axis of Fig. 3(a) corresponds to the lapse time of the receiver function. We aim to determine the depth of the Moho and its depth in our study region is around 30 to 40 km. This depth range corresponds roughly to a lapse time of 3.5 to 5 s. Thus, the parameter w is set to 1 (0 dB) for the time period up to 5 s and to −3 dB for 15 s (3×5 s).

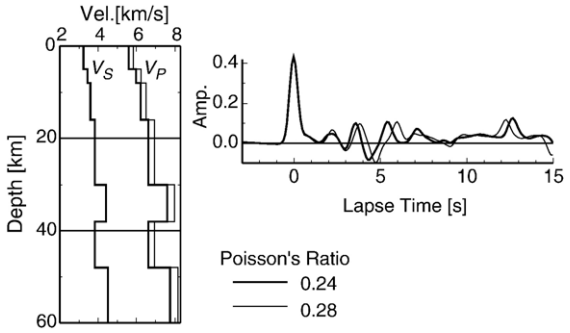

Fig. 2. Comparison between receiver functions calculated using models with different Poisson's ratios. Thick and thin lines denote the models (left) and their receiver functions (right) with Poisson's ratios of 0.24 and 0.28, respectively.

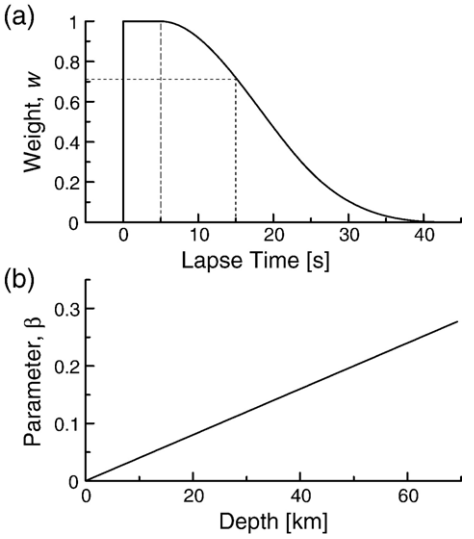

Fig. 3. Parameters used in our receiver function inversion. (a) Weighting function (w). (b) Constraint parameter (β). These parameters are sampled as discrete values in the inversion procedure.

First, we solve the following equation by using the M receiver functions to obtain the S-wave velocity model:

$$\begin{bmatrix} \mathbf{W}\cdot(\mathbf{D}_S)_1 \\ \mathbf{W}\cdot(\mathbf{D}_S)_2 \\ \vdots \\ \mathbf{W}\cdot(\mathbf{D}_S)_M \\ \beta\mathbf{I} \\ \sigma\boldsymbol{\Delta} \end{bmatrix} \cdot[\overrightarrow{s_k}] \approx \begin{bmatrix} \mathbf{W}\cdot\{(\overrightarrow{r_S})_1 + (\mathbf{D}_S)_1\cdot\overrightarrow{s_{k-1}}\} \\ \mathbf{W}\cdot\{(\overrightarrow{r_S})_2 + (\mathbf{D}_S)_2\cdot\overrightarrow{s_{k-1}}\} \\ \vdots \\ \mathbf{W}\cdot\{(\overrightarrow{r_S})_M + (\mathbf{D}_S)_M\cdot\overrightarrow{s_{k-1}}\} \\ \beta(\mathbf{I}\cdot\overrightarrow{s_0}) \\ 0 \end{bmatrix}, \tag{5}$$

where $\overrightarrow{s_k}$, $\mathbf{I}$ and $\mathbf{0}$ denote the S-wave velocity model parameters derived by the kth iteration, a unit matrix and a zero matrix, respectively. Parameter β constrains an inversion model to an initial model, and σ is a smoothing parameter. We set β as a function of depth as shown in Fig. 3(b), although Soda et al. (2001) used values of 0.3 or 0.6 for the constant β. This constraint parameter is selected by trial and error based on the synthetic test (Section 2.2). Each graph of Fig. 3 is presented as a continuous function, but we use discrete values in Eq. (5). We used the value 0.2 mainly for a smoothing parameter. If the inversion process is unstable, we select a larger value (0.25). We employed a smaller value (0.15) when the number of receiver functions applied to the inversion is less than three. Matrix $\boldsymbol{\Delta}$ is used for smoothing an estimated velocity model (Ammon et al., 1990),

$$\boldsymbol{\Delta} = \begin{bmatrix} 1 & -2 & 1 & 0 & \cdots \\ 0 & 1 & -2 & 1 & \cdots \\ 0 & 0 & 1 & -2 & \cdots \\ 0 & 0 & 0 & 1 & \cdots \\ \vdots & \vdots & \vdots & \vdots & \ddots \end{bmatrix}. \tag{6}$$

Under the assumption that an initial velocity model is close to a true model, we can numerically calculate the partial derivatives $(\mathbf{D}_S)_j$. Thus, $\overrightarrow{s_k}$ is derived from Eq. (5) by using a least-squares fitting method. Next, we calculate the $L\times L$ diagonal matrix $\mathbf{T}_{k-1}$, which consists of V_P/V_S ratios:

$$\mathbf{T}_{k-1} = \begin{bmatrix} p_{k-1}^1/s_{k-1}^1 & 0 & 0 & \cdots \\ 0 & p_{k-1}^2/s_{k-1}^2 & 0 & \cdots \\ 0 & 0 & p_{k-1}^3/s_{k-1}^3 & \cdots \\ \vdots & \vdots & \vdots & \ddots \end{bmatrix}, \tag{7}$$

where $\overrightarrow{p_k} = (p_k^1, p_k^2, \cdots, p_k^L)^t$ and $\overrightarrow{s_k} = (s_k^1, s_k^2, \cdots, s_k^L)^t$ indicate the P- and S-wave velocity model derived by the kth iteration, respectively, and the superscript t indicates transposition. We then estimate the P-wave velocity model from the following equation:

$$\begin{bmatrix} \mathbf{W}\cdot(\mathbf{D}_P)_1 \\ \mathbf{W}\cdot(\mathbf{D}_P)_2 \\ \vdots \\ \mathbf{W}\cdot(\mathbf{D}_P)_M \\ \gamma\mathbf{I} \\ \sigma\boldsymbol{\Delta} \end{bmatrix} \cdot[\overrightarrow{p_k}] \approx \begin{bmatrix} \mathbf{W}\cdot\{(\overrightarrow{r_P})_1 + (\mathbf{D}_P)_1\cdot\overrightarrow{p_{k-1}}\} \\ \mathbf{W}\cdot\{(\overrightarrow{r_P})_2 + (\mathbf{D}_P)_2\cdot\overrightarrow{p_{k-1}}\} \\ \vdots \\ \mathbf{W}\cdot\{(\overrightarrow{r_P})_M + (\mathbf{D}_P)_M\cdot\overrightarrow{p_{k-1}}\} \\ \gamma(\mathbf{T}_{k-1}\cdot\overrightarrow{s_k}) \\ 0 \end{bmatrix}. \tag{8}$$

Here, $(\mathbf{D}_P)_j$ and $(\overrightarrow{r_P})_j$ represent the same parameters as $(\mathbf{D}_S)_j$ and $(\overrightarrow{r_S})_j$, but these parameters are specifically used for P-wave velocity estimation. The parameter γ constrains an estimated V_P/V_S model to a model estimated from the S-wave velocity and V_P/V_S ratio. Since the receiver function provides very little

information regarding the P-wave velocity as compared with the S-wave velocity, we set the value of γ to 1.5 times of β. Finally, we estimate the density model $\vec{\rho}_k = (\rho_k^1, \rho_k^2, \cdots, \rho_k^L)^t$ in g/cm^3 by using Birch's law (Birch, 1961) with P-wave velocity $\vec{p}_k$ in km/s:

$$\vec{\rho}_k = 0.328\vec{p}_k + 0.613. \quad (9)$$

In many cases, the length of the residual vector decreases rapidly and the inversion models become stable after almost five iterations. In this iteration procedure, however, residuals sometimes oscillate. Hence, after 10 iterations, we select the minimum residual model as the final inversion model.

2.2. Synthetic test

In order to verify the effectiveness of our improved receiver function inversion technique, we carry out the following synthetic test. First, we design a target model, shown by the thick lines in Fig. 4(a), in which a low-velocity layer with a high Poisson's ratio exists at a depth of around 40 km. A 1-Hz Ricker wavelet with an incidence angle of 28° is used as an incident wave. We use the reflection matrix method (Kennett and Kerry, 1979) for the calculations of the structural response and the MAR model method for the receiver function estimations. The central trace (thin line with label "T") in Fig. 4(d) denotes the target "observed receiver function" estimated from the target model. We use the JMA2001 velocity model (Ueno et al., 2002) as the initial model and the thickness of each layer is set to 1 km until a depth of 40 km and to 2 km for the depth range of 40 to 60 km (shown by the thin line in Fig. 4a). Since the JMA2001 velocity model is a regional model constructed by combining artificial explosion surveys and the investigations of travel time residuals of micro-earthquakes, we use this model as the initial model in our inversion scheme. To evaluate the dependencies on the initial model, we prepare two more initial models whose velocities differ by ±5% from the JMA2001 velocity model (dashed line in Fig. 4a). The smoothing parameter σ is set to 0.15. In order to compare the synthetic result of our improved method with that of the conventional method, we assigned the same value to common parameters like σ.

The model estimated by the conventional method based on Ammon et al. (1990) is shown by the thick line

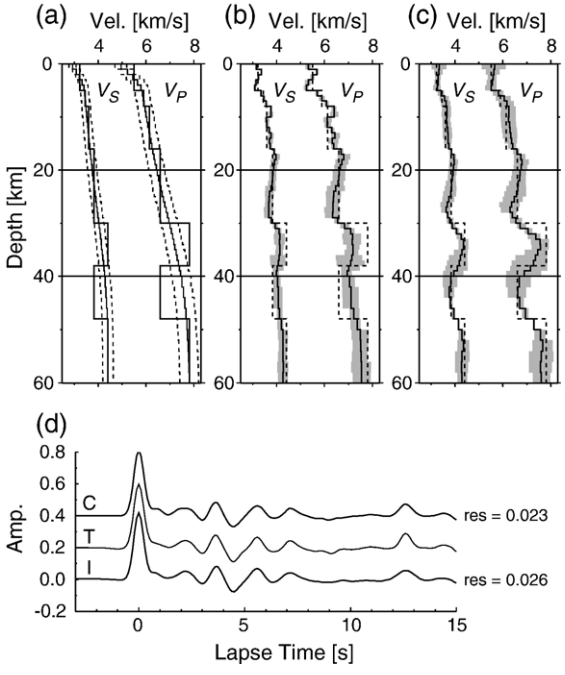

Fig. 4. (a) Target model (thick line) and initial model (thin line). Dashed lines indicate that the models fluctuated within ±5% from the initial model. (b) Model estimated by the conventional method (solid line). Dashed lines indicate the target model. Gray area represents perturbations where the velocities of the initial model fluctuate within ±5%. (c) The same as in (b), but the solid line indicates the model estimated by our improved inversion method. (d) Comparison between synthetic receiver functions. The uppermost trace labeled as "C" and the lowermost trace labeled as "I" denote the receiver functions calculated from the estimated velocity model shown by solid lines in (b) and (c), respectively. Middle trace labeled as "T" indicates the target receiver function. Parameter *res* shown at the right of the receiver function indicates the residual in seconds.

in Fig. 4(b) and the receiver function estimated from this model is indicated as the uppermost trace, labeled as "C" in Fig. 4(d). The gray area in Fig. 4(b) represents perturbations where the velocity of the initial model differs by 5% from the JMA2001 velocity model. The model estimated by the improved method and its receiver function are shown in Fig. 4(c) and the lower trace labeled "I" in Fig. 4(d), respectively. The residual is shown to the right of each estimated receiver function. Both the conventional method as well as our improved method reconstructs the velocity discontinuity at a depth of 30 km. Both the estimated receiver functions are suitably consistent with the target receiver function and the residuals are almost equal. However, the model estimated by the conventional method does not show a clear low-velocity layer. One reason for this shortcoming is the strong constraint to the Poisson's ratio and the other is that the conventional method does not consider the lapse time weight *w*. Although the inversion structure calculated by our method exhibits a slight dependency of the initial model on velocity discontinuities, the estimated model is considerably closer to the pre-design target model than the conventional method.

3. Data

For the receiver function estimation, we use the teleseismic waveform data recorded at the 125 Hi-net stations in southwestern Japan, as shown in Fig. 1. Each Hi-net station is equipped with a three-component short-period velocity seismometer at the bottom of a borehole —the depth of which exceeds 100 m (Okada et al., 2004). In order to avoid the contamination of surface reflection and other high frequency noise, we select stations with sensor depths shallower than 350 m and apply a Gaussian low-pass filter with a cut-off frequency of 0.6 Hz. In addition, to eliminate low-frequency noise, a high-pass filter with a corner frequency of 0.1 Hz is applied to raw seismograms with the instrument response correction. Previously, Shiomi et al. (2004) estimated receiver functions using Hi-net waveform data of teleseisms with magnitudes of 5.5 or greater. In this study, in order to improve the signal-to-noise ratio, we analyze a total of 109 records of teleseismic events from October 2000 to April 2004 that have magnitudes of 6.0 or greater and epicentral distances between 30° and 90°. Fig. 5 shows the epicenter distribution of the events used in this study. A total of 653 receiver functions are used to estimate velocity models.

It is difficult to determine whether or not the Moho beneath southwestern Japan is flat from previous results such as those of Zhao et al. (1992) and Ryoki (1999). If a dipping velocity boundary exists, the receiver functions would vary with the back azimuth (e.g., Ferris et al., 2003; Shiomi et al., 2004). In order to improve the information obtained from the converted phases and to

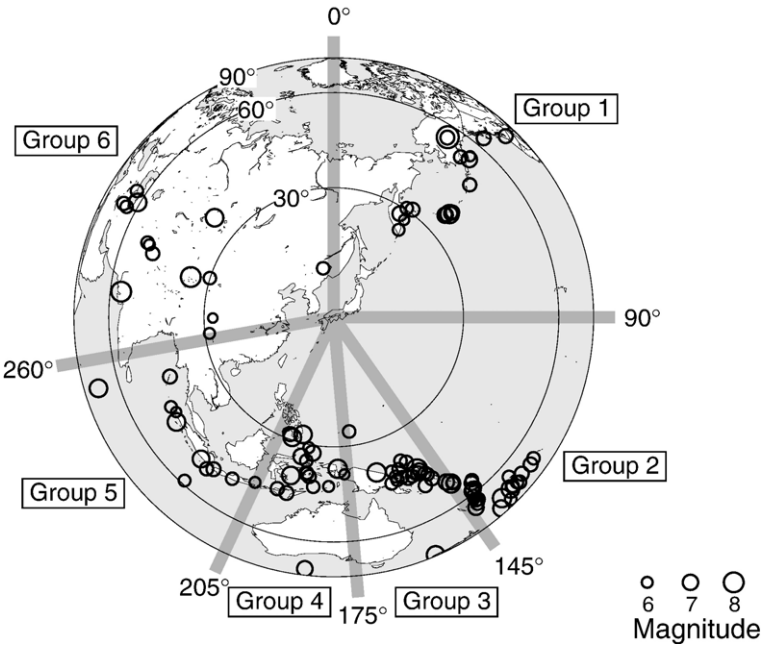

Fig. 5. Epicenter distribution of the 109 teleseismic events used in this study. Gray lines indicate the boundaries between the event-groups used in the inversion analysis. Group indexes are indicated in boxes.

avoid contamination arising from the dipping structure, we classify the estimated receiver functions into six groups according to the back azimuth of each station. We then carry out an inversion of every group of the receiver functions to obtain the seismic velocity structure. The classification and index of each group are shown in Fig. 5.

4. Results

4.1. Inverted velocity model

Fig. 6 presents examples of the estimated receiver functions at stations OKYH, MKWH and UWAH (see Fig. 1), where the left and right panels show the radial and transverse component receiver functions, respectively. The lapse time of a receiver function is converted to depth by using the JMA2001 velocity model in this figure. Each receiver function clearly demonstrates its dependence on back azimuth (BAZ). For the radial receiver functions of the northern direction at OKYH, later phases appear at depths of 30 and 40 km. These phases are combined at a depth of 35 km at the southern part of OKYH. At a 35-km depth of the transverse components for the southern earthquakes, certain later phases are not detected, although the transverse receiver functions for the east and west directions have weak phases. This means that two velocity discontinuities exist beneath OKYH; these dip toward the south or north. At MKWH and UWAH, a distinct later phase exists at a depth of 40 to 45 km. At a depth of 45 km, the phases of the transverse receiver functions at UWAH change from negative to positive at 135° in back azimuth. Thus, the dip direction of the discontinuity beneath UWAH is northwest.

For the receiver functions indicated by the half-square bracket at the bottom of the left panel of Fig. 6, we invert for velocity models shown by the solid lines in Fig. 7(a). As mentioned above, the JMA2001 velocity model is used as the initial model. The gray area in Fig. 7(a) indicates perturbations where the velocities of the initial model fluctuate within ±5%. The thickness of each layer is set to 1 km until a depth of 40 km and to 2 km for the depth range of 40 to 60 km. Fig. 7(b) shows the comparisons between the observed receiver functions (thin lines) and synthetic receiver functions calculated from the inversion model (thick lines). The ray parameter p and residual *res* are indicated to the right of each receiver function. Synthetic receiver functions are well reproduced for each station and ray parameter. The estimated velocity model at each station shows velocity changes at the depth range of 35 to 40 km. Only one velocity discontinuity, indicated by the arrow with labeled as “M” in Fig. 7(a), is found at the OKYH and UWAH stations. This discontinuity corresponds to the Moho beneath each station. Although the dependence on the initial model is not small, we observe two discontinuities–“M1” and “M2”–at station MKWH where a 10-km-thick low-velocity layer lies between these two discontinuities. This low-velocity layer (LV) may correspond to the subducting oceanic crust in the PHS; hence, the upper boundaries of the high-velocity

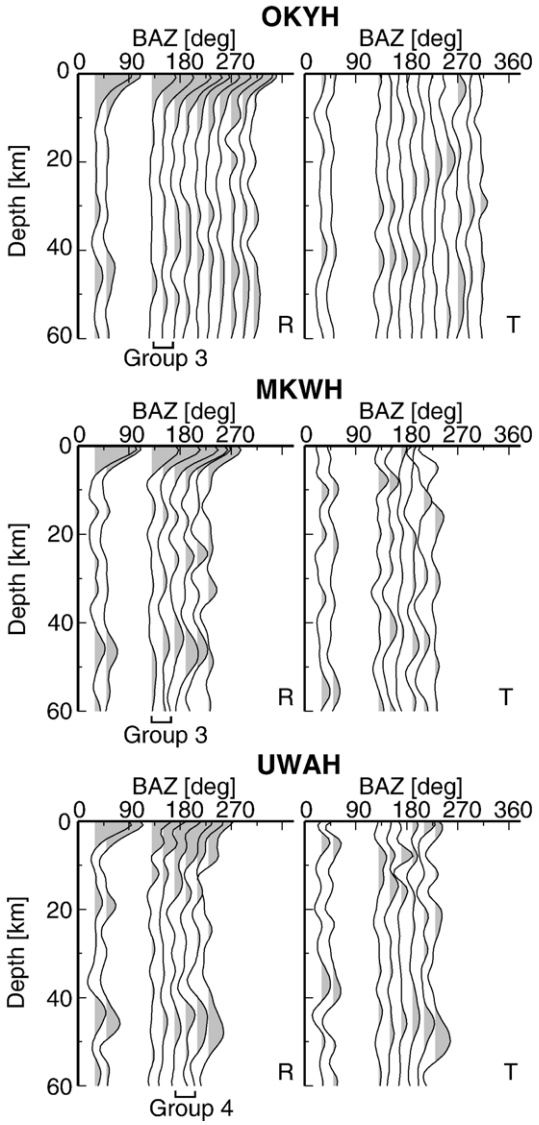

Fig. 6. Examples of estimated receiver functions for the three stations shown in Fig. 1. Time is converted into depth by using the JMA2001 velocity model and the horizontal axis is the back azimuth (BAZ). Labels “R” and “T” represent the radial and transverse components, respectively.

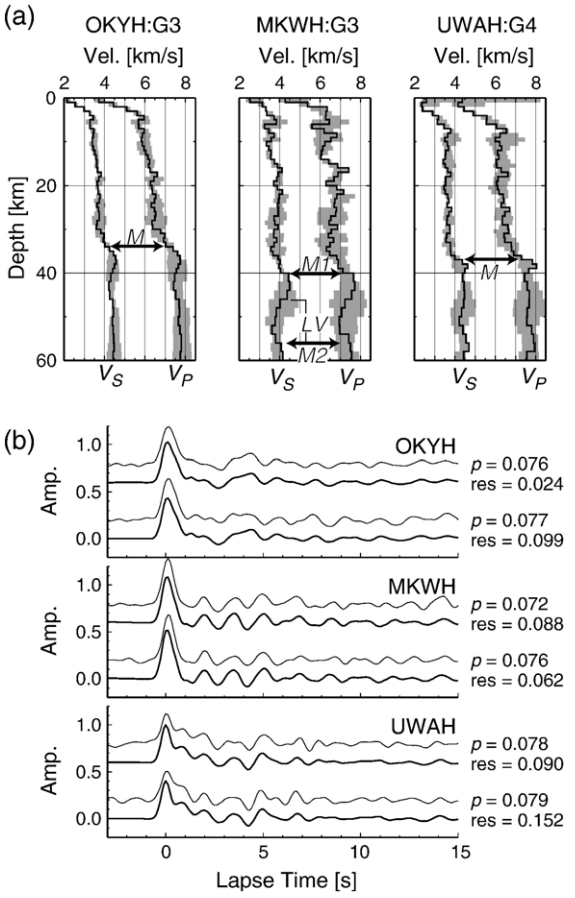

Fig. 7. (a) Examples of estimated velocity structures (solid lines) at the same stations in Fig. 6. The receiver functions used for the velocity inversion are indicated by the horizontal half-square bracket at the bottom of Fig. 6. Notation is the same as for Fig. 4(b). Arrows with label "M" (M1, M2) indicate the distinct velocity gap corresponding to the Moho. "LV" indicates the existence of the low velocity layer. (b) Examples of observed (thin line) and estimated (thick line) receiver functions for each station in (a). Parameters *p* and *res* attached to each receiver function indicate the ray parameter and the residual, respectively.

layers above and below the oceanic crust can be recognized as the continental Moho (M1) and the subducting oceanic Moho (M2), respectively. The oceanic crust lying beneath the continental Moho is detected only at the stations located around the central Chugoku region; further, the depth of the upper boundary of the low-velocity layer is 45 to 50 km.

4.2. Depth contour of the Moho

The Moho is defined as a seismic velocity discontinuity at which the P-wave velocity exceeds around 7.8 km/s in deeper portions. This P-wave velocity corresponds to an S-wave velocity of approximately 4.5 km/s. However, as shown in Fig. 7(a), the estimated velocity models sometimes do not present the Moho as a clear velocity boundary because we adopt the smoothing parameter σ in our inversion process. In this study, the Moho is defined as the depth at which the S-wave velocity changes from 3.7 to 4.5 km/s and at which the velocity gradient shows a maximum value. If two clear velocity discontinuities exist, we select both discontinuities. Following this definition, we note the Moho depth from the estimated velocity models at each station. Next, we map the P-to-S conversion depth at the Moho to a point along the ray path using our inversion model. For the cases when the velocity gradient of the estimated model is smaller than 0.2 [/s], the estimated model is unstable, or the average residual is greater than 0.2 s, we avoid using the data. Fig. 8 shows the example of an unstable inversion result. The radial receiver functions shown in Fig. 8(a) indicate clear velocity discontinuities at depths of 15, 25 and 40 km. However, in group 5 (G5), the amplitude of the phase at 40 km is larger than that in the other direction. Considering the transverse components, the underground structure at the southwestern direction of SJOH may contain strong inhomogeneities. Thus, it is hard to estimate a stable velocity model for this direction, although the estimated model shown in Fig. 8(b) includes some velocity discontinuities.

We finally select a total of 524 models. Fig. 9 shows the distribution of the conversion points at the Moho as well as its vertical cross sections along the two lines A and B. The conversion points beneath Shikoku, represented by inverted triangles, are consistently dipping down from the south to the north with a low dip angle (Fig. 9b). These conversion points correspond to the oceanic Moho of the subducting PHS estimated by Shiomi et al. (2004) (represented by gray lines in Fig. 9b). The conversion points beneath the Chugoku region, represented by solid triangles, are also continuously distributed and are almost flat at a depth of 30 to 40 km. These points are classified as the continental Moho. From profiles like Fig. 9(b), it becomes clear that the Moho at OKYH and UWAH, represented by arrows and labeled as "M" in Fig. 7(a), indicate the continental and oceanic Moho, respectively. Beneath the Seto Inland Sea (34.1°N to 34.7°N), both the continental and oceanic Moho are detected separately. Assuming that each Moho is continuous, we classify all the conversion points as continental and oceanic Moho.

Fig. 10 shows the depth distribution of the continental and oceanic Moho. These contour maps are constructed by spatially interpolating the depth of

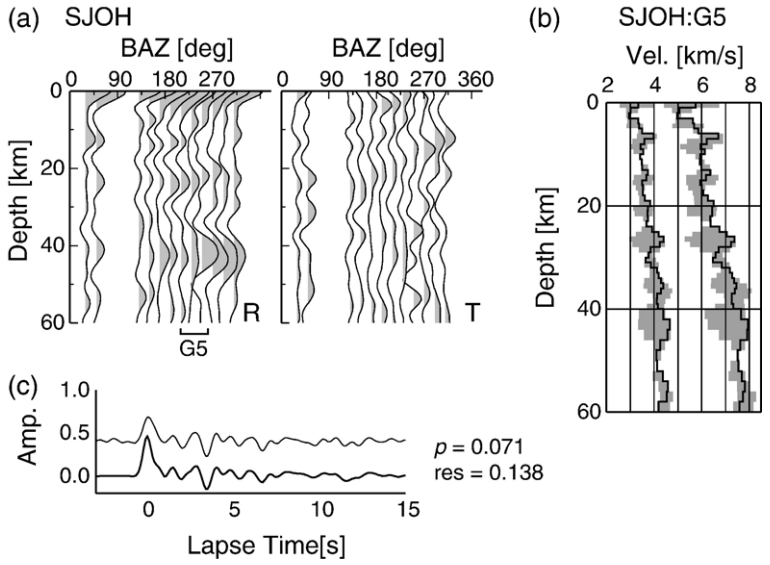

Fig. 8. (a) Examples of estimated receiver functions at SJOH shown in Fig. 1. (b) Examples of the estimated structure of group 5 at SJOH. (c) Comparison between observed (thin line) and estimated (thick line) receiver functions. Notation is the same as for Figs. 6 and 7.

the conversion points based on the nearest neighbor averaging method with a search radius of 15 km (e.g., Wessel and Smith, 1998). The continental Moho is mainly detected beneath the Chugoku region. It is located at a depth of about 30 km beneath the coast of the Sea of Japan in the north and the Seto Inland Sea coast in the south and is relatively deeper in the central part of the Chugoku region. The oceanic Moho is clearly detected beneath Shikoku and the southern Chugoku region. It is about 25 km deep beneath the Pacific coast and dips down toward the northwest. The oceanic Moho extends at least to 34.5°N and attains a depth of about 60 km. The oceanic Moho is not detected beneath the northeastern part of our study region.

5. Discussion

The Bouguer gravity anomaly distribution in the study region is shown in Fig. 11(a) (GSJ and KIGAM, 2002). Fig. 11(b)−(d) represent vertical cross sections along the profile line A−a in Fig. 11(a) of the surface topography (b), gravity anomaly (c) and Moho depth (thick line) with receiver function amplitude (d). The horizontal distance in Fig. 11(b), (c) and (d) is measured from the point A to a, as shown in Fig. 11(a). Beneath the mountain area at the central part of Chugoku (a distance of 30 to 80 km) and the Shikoku region (a distance of 180 to 220 km), the Moho becomes deeper. The depth variation of the Moho shows very good agreement with not only the topography but also the gravity anomaly variation. These features correspond well to the concept of isostasy. Hori et al. (1985) stated that the subducting oceanic lithosphere immediately below the continental Moho causes a negative gravity anomaly. In Fig. 11, the gravity anomaly is relatively small around the attached region between the oceanic crust and the continental lower crust (a distance of 200 km). Thus, this characteristic indicates that the gravity anomaly around Shikoku Island is strongly affected by the existence of the subducting PHS. In Fig. 11(d), the lapse time of the receiver function is converted into depth by using our estimated velocity models. The red blocks indicate the presence of a seismic velocity gap, where the deeper layer has a higher velocity than the shallower one. The Moho depth estimated by this study is in good agreement with these red blocks of the receiver function amplitude.

In Fig. 11(e), we show the interpolated S-wave velocity structure derived from the receiver function inversions and hypocenters of microearthquakes determined by the Japan Meteorological Agency (JMA), after interpolation by the nearest neighborhood technique with a search radius of 15 km. The JMA2001 velocity model is used for locating the hypocenter and as the initial model of our inversion process. The hypocenter location error is mainly within 1 km in the horizontal direction and 2 km in depth beneath the inland area. Beneath the Chugoku region, shown by box B in Fig. 11(e), the distribution of microearthquakes becomes slightly deeper in the area where the low-velocity layer (about 3.4 km/s, indicated in orange in Fig. 11e) is relatively thicker. In the Shikoku region,

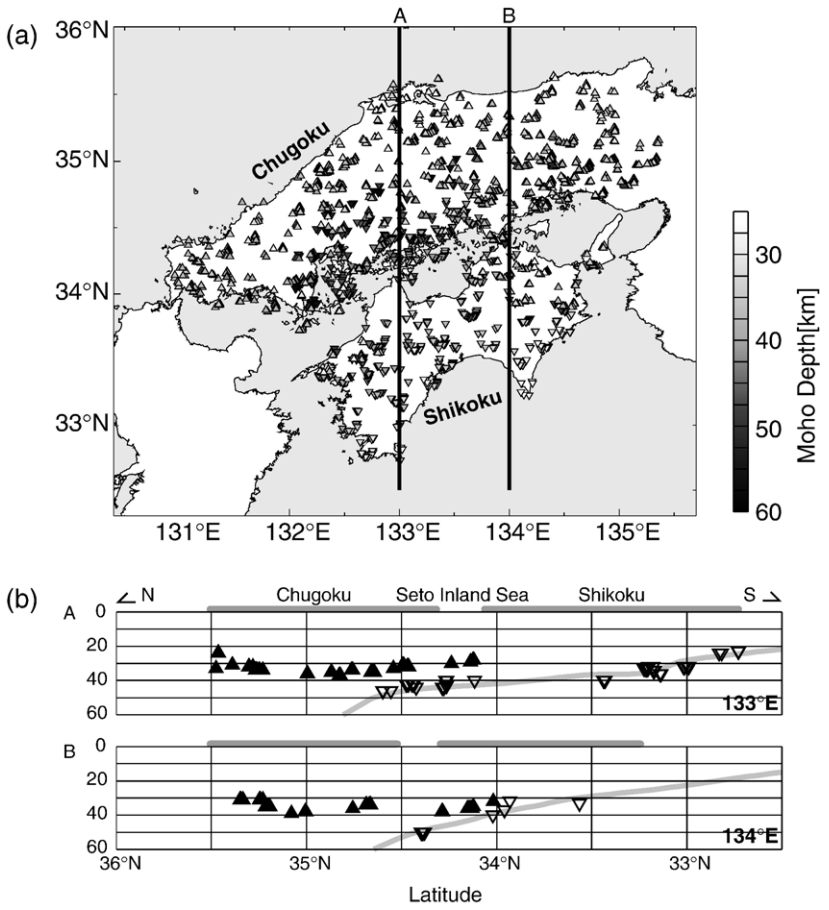

Fig. 9. (a) Distribution of the P-to-S conversion points at the Moho. Triangles and inverted triangles denote the conversion points at the continental and oceanic Moho, respectively. Moho depth at each conversion point is shown by the density scale. (b) Vertical cross sections of the conversion points at the Moho along the thick lines A and B in (a). Solid triangles and open inverted triangles indicate the conversion points at the continental and oceanic Moho, respectively. Gray lines denote the oceanic Moho estimated from the depth converted receiver function amplitude (Shiomi et al., 2004).

the low-velocity anomaly exists at a distance of 180 km from A and at a depth of 15 km. The active seismic zone is located to the south of this low-velocity anomaly; further, few earthquakes occur in and around this anomaly (box C in Fig. 11e). Consequently, we state that the distribution of crustal earthquakes corresponds well with the velocity fluctuations. This is despite the fact that this study employs only teleseismic waves and our resultant S-wave model is different from the JMA2001 velocity model. The correlation between seismic velocity perturbations and seismicity has been reported both in California and the Japan Islands (e.g., Lees and Nicholson, 1993; Matsubara et al., 2003) based on high-resolution travel time tomography. Our result from the receiver function analysis shows a similar relationship. These results are evidence that the occurrence of crustal earthquakes is selective and greatly influenced by local seismic velocity fluctuations.

Fig. 12 is a comparison between the results of this study and those obtained from artificial explosion surveys in southwestern Japan. For the profile A−a in Fig. 12(b), referred to as the Kurayoshi-Hanabusa line, the Moho estimated by Yoshii et al. (1974) (represented by a thick black line) shows very good agreement with the continental Moho geometry constructed in this study (a light gray line). For the Iejima-Torigatayama line shown in Fig. 12(c), the thick black line, which represents the Moho proposed by Ito et al. (1982), shows a dip from northeast to southwest. This dip direction is not consistent with that of the PHS subducting from south to north. According to our results, the northeastern portion of the Moho estimated by Ito et al. (1982) corresponds to the continental Moho

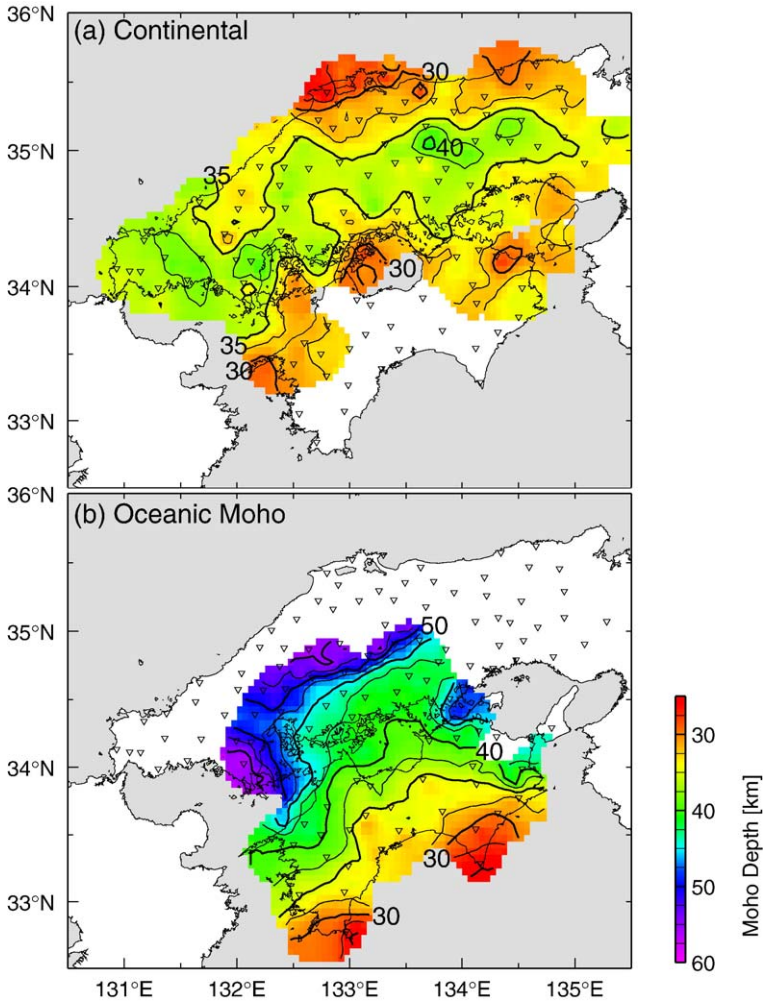

Fig. 10. Depth distribution of the (a) continental and the (b) oceanic Moho. The Moho depth is shown by the color scale and contours with an interval of 5 km. Inverted triangles denote the locations of the Hi-net stations used in this study.

(light gray line), while the southwestern portion corresponds to the oceanic Moho (dark gray line). Near the vicinity point of the two Mohos, around 34°N (a distance of 100 km), the continental Moho is slightly shallower than the oceanic Moho. Thus, the contradiction between Ito et al. (1982) and the dip direction of the PHS can be attributed to the fact that the former did not distinguish between the continental and the oceanic Moho. Recently Salah and Zhao (2004) analyzed the travel time of the direct wave and the Moho-reflected phases recorded at the Hi-net stations and constructed Moho depth variations beneath the eastern part of the Chugoku and Shikoku regions. They insist that the maximum depth of the Moho estimated by SmS and S phases is located at 35°N and 133.8°E at a depth of 32 km. The depth variation of their model exhibits a similar tendency as the continental Moho geometry determined by us; however, we estimate that the maximum depth is 40 km or deeper. Since they attempted to represent the Moho depth variation using a polynomial, their model may be strongly smoothed.

We constructed numerous vertical profiles, shown in Fig. 9(b), in order to estimate the area where the continental lower crust and the oceanic crust overlap. Fig. 13(a) is a schematic illustration of a north-to-south profile in southwestern Japan. The circle indicates the southern edge of the continental Moho detected in this study, while the square indicates a point on the oceanic Moho at the same depth as that indicated by the circle. The star indicates the northern bound of the region, where the continental crust is in contact with the oceanic one. Since the resolution is not sufficient, we cannot accurately determine the location of the star. After noting the positions of the circles and squares

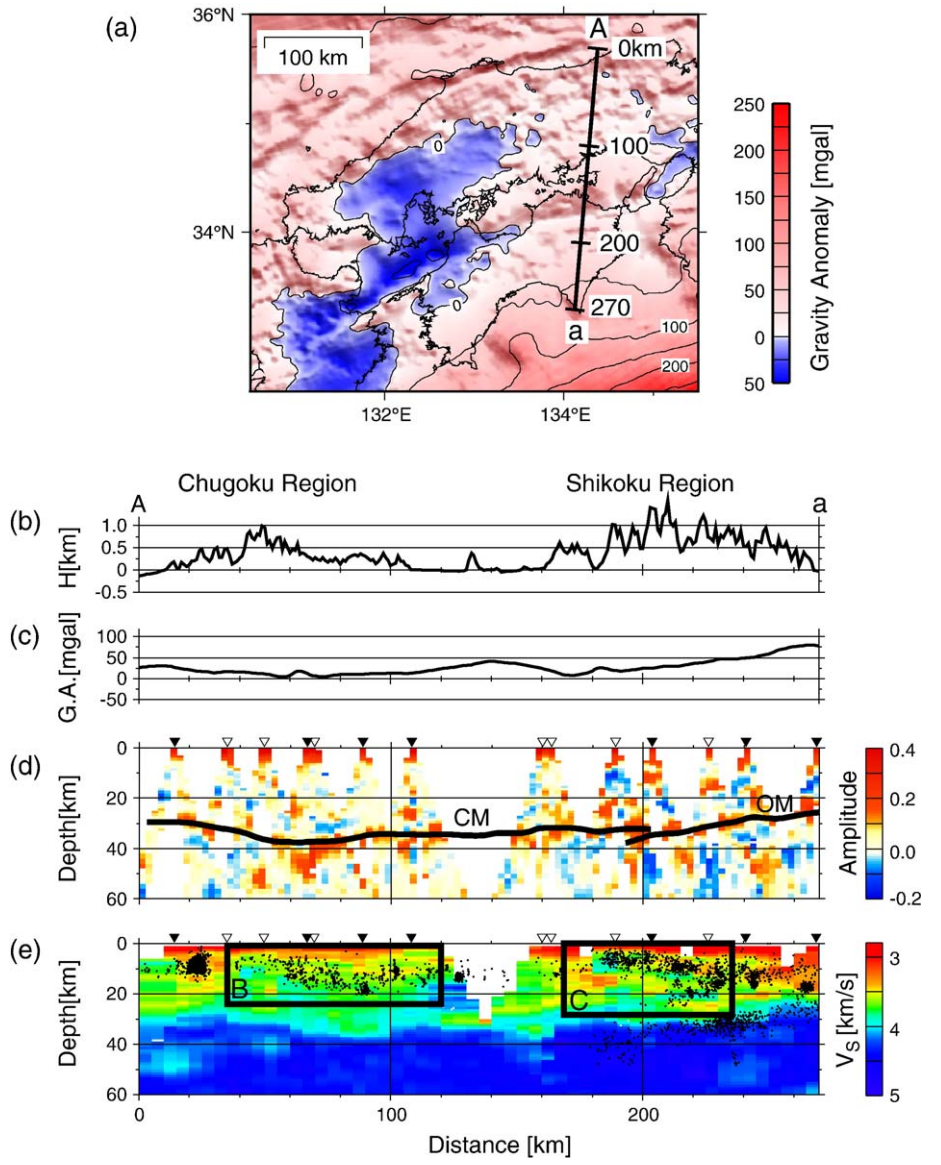

Fig. 11. (a) Bouguer gravity anomaly map of southwestern Japan (after GSJ and KIGAM, 2002). The contour interval is 50 mgal. Thick line A–a indicates the location of the vertical cross section shown in (b) to (e). (b) Vertical cross section of the surface topography, *H*. (c) Vertical cross section of the Bouguer gravity anomaly. (d) Vertical cross section of the depth-converted receiver function amplitude. The depth profile of each Moho estimated by this study is shown by a thick line. CM and OM represent the continental and oceanic Moho, respectively. Solid and open triangles at the top of the panel indicate the locations of stations that are within 5 km and 15 km, respectively, from the profile line. (e) Interpolated S-wave velocity estimated by receiver function inversion. Black dots indicate hypocenters of microearthquakes with magnitude 0.0 or larger according to the hypocentral catalogue of the Japan Meteorological Agency (JMA).

from the vertical profiles, we map the trace of the circles (thick line) and that of the squares (thin line), as shown in Fig. 13(b). The northern bound of the attached region (star in Fig. 13a) should be located between the two solid lines in Fig. 13(b). Based on the analysis of the later phases of the local seismograms, Ohkura (2000) estimated the northern bound of the overlapping region of the continental and oceanic crusts shown by the dashed line in Fig. 13(b). His result shows a simple feature and suggests that the Moho beneath Shikoku is primarily the oceanic one. On the contrary, our result indicates that the northern bound of the overlapping region bends and a wedge-shaped mantle may exist between the continental crust and the subducting slab

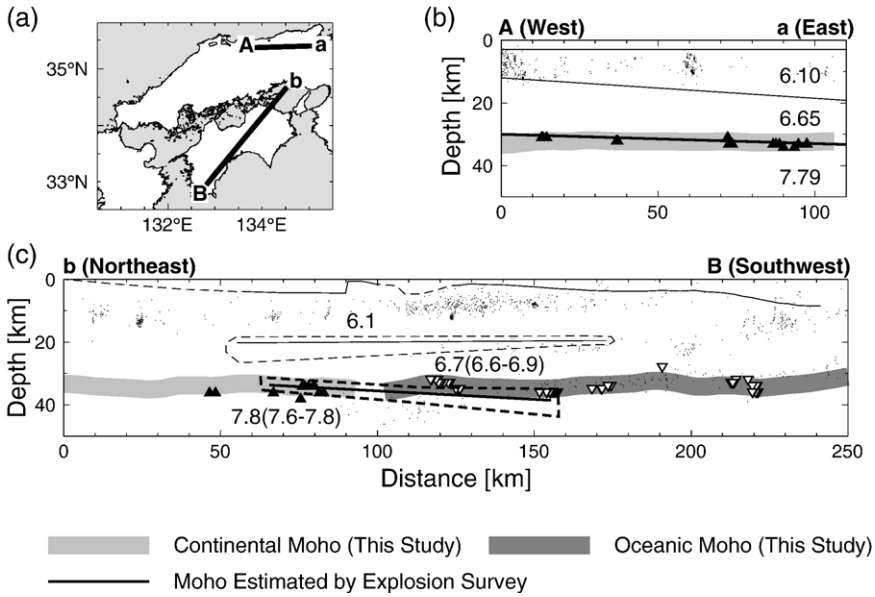

Fig. 12. Comparison between the Moho depth variation derived from this study and that from artificial explosion surveys. (a) Location map of the cross sections. (b) Kurayoshi-Hanabusa line. Solid triangles and the light gray line denote the conversion point at the continental Moho and its geometry estimated by this study. The thick and thin lines indicate the Moho and other velocity boundaries estimated by Yoshii et al. (1974). P-wave velocities by Yoshii et al. (1974) are shown in km/s. Dots indicate hypocenters of microearthquakes with magnitudes of 0.0 or greater, according to the hypocentral catalogue of the JMA. (c) Iejima-Torigatayama line. The open inverted triangle and dark gray line denote the conversion point at the oceanic Moho and its geometry estimated by this study. Dotted line indicates the possible range of each boundary. Other notations are the same as (b), but the result of the artificial survey is based on Ito et al. (1982).

beneath the western and eastern parts of Shikoku. This characteristic corresponds well to the other geophysical features. As shown in Fig. 11(a), the Bouguer gravity anomaly is locally positive at the Sadamisaki Peninsula, western part of Shikoku (see Fig. 13b), although the eastern part of the peninsula shows a negative value. This anomaly distribution supports the concept of the existence of a mantle wedge beneath the peninsula since the positive gravity anomaly is caused by the existence of high-density material near the ground surface. On the other hand, megathrust earthquakes have repeatedly occurred in this region (Ando, 1975). Fig. 13(b) also shows the coseismic slip area of the 1946 Nankai earthquake (M_W 8.3), where the slip is 1 m or more (Baba et al., 2002). According to Baba et al. (2002), a large coseismic slip is estimated at the inland area of the Shikoku Island. The northern bound of the overlapping region estimated in this study shows good coincidence with the distribution of the coseismic slip (Fig. 13b) and the downdip limit of the estimated source region of the next anticipated Nankai earthquake (The Headquarters for Earthquake Research Promotion, 2001). This characteristic indicates that the interplate coupling might be affected by the configuration of the continental and oceanic Moho.

As shown in Fig. 8(b), conversion point data is rather sparse around the region between 33.5°N and 34.0°N for profile A as well as 34.2°N and 34.6°N for profile B, where the continental and oceanic Moho might exist in close proximity. The deficiency of data may not be fully attributable to the relatively poor distribution of seismograph stations. Bostock et al. (2002) found that the continental Moho becomes unclear and indicated that the reflection coefficients at the Moho change from positive to negative near the subducting slab. They also discovered that a low S-wave velocity region exists in the forearc mantle beneath the southern Cascadia subduction zone. They maintained that the existence of a serpentinized cold mantle was primarily responsible for this feature. In southwestern Japan, Obara (2002) observed non-volcanic long-period tremors that occurred along the subducting PHS and stated that the origin of these tremors may be related to fluid generated from the slab due to dehydration processes. In this study, although we did not detect “the inverted Moho” that was reported by Bostock et al. (2002), the estimated models show an unclear velocity gap at around the region where the two types of Moho exist in close proximity that. From our results, combined with the facts reported by Bostock et al. (2002) and Obara (2002), we can state that

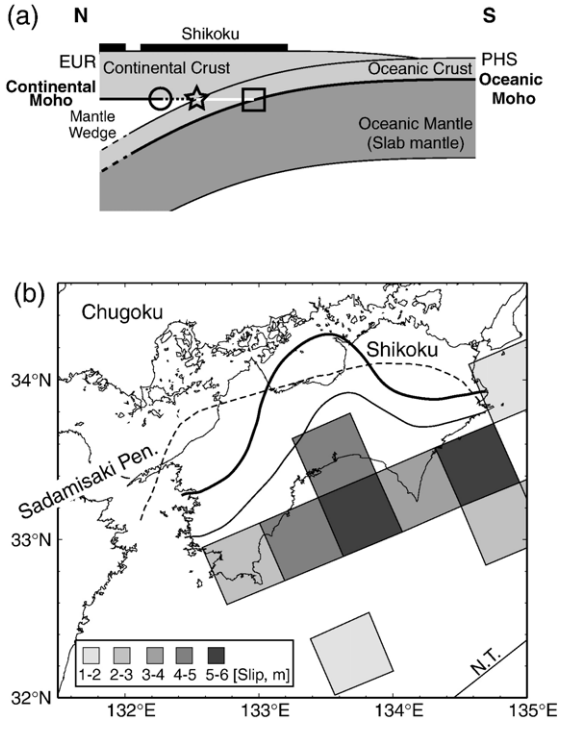

Fig. 13. (a) Schematic illustration of the underground structure beneath southwestern Japan, where "PHS" and "EUR" refer to the Philippine Sea plate and the Eurasian plate, respectively. Circle, star and square indicate the detected southern edge of the continental Moho, northern bound of the region where the continental lower crust and the subducting oceanic crust overlap, and a point on the oceanic Moho located at the same depth as the circle, respectively. Dashed lines represent the unclear parts in our analysis. (b) Overlapping region between the continental and the oceanic crusts. The southern edge of the continental Moho detected in this study is indicated by the thick line. Thin line denotes the trace of the oceanic Moho at the same depth as the southern edge of the continental Moho. In the vertical profile shown in (a), the thick line and the thin line correspond to the circle and the square, respectively. Dashed line denotes the northern edge of the attached region based on the analysis of the later phases of the local seismograms (Ohkura, 2000). Shaded area indicates the region where a coseismic slip of 1 m or more occurred after the 1946 Nankai earthquake (Baba et al., 2002).

a mantle wedge exists beneath southwestern Japan and it may be cold and serpentinized.

6. Conclusions

In this study, we estimated a detailed velocity structure and constructed a detailed depth contours of the continental and oceanic Moho beneath southwestern Japan from inversion models based on receiver functions. In order to properly determine a shallow velocity structure, we improved upon the method for linearized time-domain receiver function inversion, in which we adopt a weighting function without fixing the value of the Poisson's ratio. From the synthetic test, we confirmed that this improved inversion method is more effective than the conventional one. According to the estimated models, a 10-km-thick low-velocity layer exists under the continental Moho at the stations in the southern part of the Chugoku region. The depth of the upper boundary of the low-velocity layer is between 45 and 50 km. This layer corresponds to the subducting oceanic crust of the PHS and the oceanic Moho is clearly identified as the bottom of the oceanic crust. By classifying the P-to-S conversion points at the Moho and by interpolating, we were able to separately draw the depth contours of the continental and oceanic Mohos. We observed that the subducting oceanic Moho dips down from the south to the northwest, exhibiting complicated features. The oceanic Moho extends at least to 34.5°N with a depth of around 60 km beneath the central part of the Chugoku region. The continental Moho is relatively shallower beneath the coast of the Sea of Japan and the Seto Inland Sea; however, its depth increase to more than 40 km around 35.0°N and 133.8°E. Both continental and oceanic Moho configurations satisfy the concept of isostasy well. We also demonstrated that the oceanic crust is in contact with the continental lower crust beneath the southern and central Shikoku region and that a mantle wedge exists beneath the eastern and western part of Shikoku. This feature is in good agreement with the gravity anomaly distribution and downdip limit of a slip area of a megathrust earthquake. The perturbation of the estimated velocity models shows a good correlation with the distribution of the microearthquakes. This feature strongly indicates that the occurrence of earthquakes is greatly affected by local velocity fluctuations.

Acknowledgements

We thank Anshu Jin, Masakazu Ohtake, Andrew Frederiksen and anonymous reviewer who kindly provided many useful comments. We are grateful to Charles J. Ammon for providing the receiver function inversion software. We also thank the Japan Meteorological Agency and the Ministry of Education, Culture, Sports, Science and Technology, Japan for providing hypocentral data. We used the GMT software (Wessel and Smith, 1998) for drawing the figures.

References

Ammon, C.J., Randall, G.E., Zandt, G., 1990. On the nonuniqueness of receiver function inversions. J. Geophys. Res. 95 (B10), 15303–15318.

Ando, M., 1975. Source mechanism and tectonic significance of historical earthquakes along the Nankai Trough, Japan. Tectonophysics 27, 119–140.

Baba, T., Tanioka, Y., Cummins, P.R., Uhira, K., 2002. The slip distribution of the 1946 Nankai earthquake estimated from tsunami inversion using a new plate model. Phys. Earth Planet. Inter. 132, 59–73.

Birch, F., 1961. The velocity of compressional waves in rocks to 10 kilobars. J. Geophys. Res. 66, 2199–2224.

Bostock, M.G., Hyndman, R.D., Rondenay, S., Peacock, S.M., 2002. An inverted continental Moho and serpentinization of the forearc mantle. Nature 417, 536–538.

Chang, S.-J., Baag, C.-E., Langston, C.A., 2004. Joint analysis of teleseismic receiver function and surface wave dispersion using the genetic algorithm. Bull. Seismol. Soc. Am. 94 (2), 691–704.

Du, Z.J., Foulger, G.R., 1999. The crustal structure beneath the northwest fjords, Iceland, from receiver functions and surface waves. Geophys. J. Int. 139, 419–432.

Ferris, A., Abers, G.A., Christensen, D.H., Veenstra, E., 2003. High resolution image of the subducted Pacific (?) plate beneath central Alaska, 50–150 km depth. Earth Planet. Sci. Lett. 214, 575–588.

Galvé, A., Sapin, M., Hirn, A., Diaz, J., Lépine, J.-C., Laigle, M., Gallart, J., Jiang, M., 2002. Complex images of Moho and variation of Vp/Vs across the Himalaya and south Tibet, from a joint receiver-function and wide-angle-reflection approach. Geophys. Res. Lett. 29 (24), 2182. doi:10.1029/2002GL015611.

GSJ and KIGAM (Eds.), 2002. Geoscientific maps of southern part of Korea, western part of Japan and their adjoining seas (CD-ROM), Digital Geoscience Map, P-4, AIST, Japan.

Helmberger, D.V., Wiggins, R., 1971. Upper mantle structure of midwestern Unites States. J. Geophys. Res. 76 (14), 3229–3245.

Hirahara, K., 1981. Three-dimensional seismic structure beneath southwest Japan: the subducting Philippine Sea plate. Tectonophysics 79, 1–44.

Honda, S., Nakanishi, I., 2003. Seismic tomography of the uppermost mantle beneath southwestern Japan: seismological constraints on modeling subduction and magmatism for the Philippine Sea slab. Earth Planets Space 55, 443–462.

Hori, S., Inoue, H., Fukao, Y., Ukawa, M., 1985. Seismic detection of the untransformed 'basaltic' oceanic crust subducting into the mantle. Geophys. J. R. Astron. Soc. 83, 169–197.

Ito, K., Yoshii, T., Asano, S., Sasaki, Y., Ikami, A., 1982. Crustal structure of Shikoku, southwestern Japan as derived from seismic observations of the Iejima and the Torigatayama explosions. ZISIN2 35, 377–391 (in Japanese with English abstract).

Kamiya, S., Kobayashi, Y., 2000. Seismological evidence for the existence of serpentinized wedge mantle. Geophys. Res. Lett. 27 (6), 819–822.

Kennett, B.L.N., Kerry, N.J., 1979. Seismic waves in a stratified half space. Geophys. J. R. Astron. Soc. 57, 557–583.

Kodaira, S., Kurashimo, E., Park, J.-O., Takahashi, N., Nakanishi, A., Miura, S., Iwasaki, T., Hirata, N., Ito, K., Kaneda, Y., 2002. Structural factors controlling the rupture process of a megathrust earthquake at the Nankai Trough seismogenic zone. Geophys. J. Int. 149, 815–835.

Kurashimo, E., Tokunaga, M., Hirata, N., Iwasaki, T., Kodaira, S., Kaneda, Y., Ito, K., Nishida, R., Kimura, S., Ikawa, T., 2002. Geometry of the subducting Philippine Sea plate and the crustal and upper mantle structure beneath eastern Shikoku Island revealed by seismic refraction/wide-angle reflection profiling. ZISIN2 54, 489–505 (in Japanese with English abstract).

Lees, J.M., Nicholson, C., 1993. Three-dimensional tomography of the 1992 southern California earthquake sequence: constraints on dynamic earthquake rupture? Geology 21, 387–390.

Li, X., Sobolev, S.V., Kind, R., Yuan, X., Estabrook, Ch., 2000. A detailed receiver function image of the upper mantle discontinuities in the Japan subduction zone. Earth Planet. Sci. Lett. 183, 527–541.

Matsubara, M., Sekine, S., Obara, K., Kasahara, K., 2003. Low-velocity oceanic crusts at the top of subducting plates beneath Japan Islands imaged by tomographic method using the NIED Hi-net data. EOS Trans. AGU 84 (46) Fall Meet. Suppl., Abstract T52B-0256.

Obara, K., 2002. Nonvolcanic deep tremor associated with subduction in southwest Japan. Science 296, 1679–1681.

Ohkura, T., 2000. Structure of the upper part of the Philippine Sea plate estimated by later phases of upper mantle earthquakes in and around Shikoku, Japan. Tectonophysics 321, 17–36.

Okada, Y., Kasahara, K., Hori, S., Obara, K., Sekiguchi, S., Fujiwara, H., Yamamoto, A., 2004. Recent progress of seismic observation networks in Japan—Hi-net, F-net, K-NET and KiK-net. Earth Planets Space 56, xv–xxviii.

Oleskevich, D.A., Hyndman, R.D., Wang, K., 1999. The updip and downdip limits to great subduction earthquake: thermal and structural models of Cascadia, south Alaska, SW Japan, and Chile. J. Geophys. Res. 104 (B7), 14965–14991.

Ryoki, K., 1999. Three-dimensional depth structure of the crust and uppermost mantle beneath southwestern Japan and its regional gravity anomalies. ZISIN2 52, 51–63 (in Japanese with English abstract).

Salah, M.K., Zhao, D., 2004. Mapping the crustal thickness in southwest Japan using Moho-reflected waves. Phys. Earth Planet. Inter. 141, 74–94.

Shiomi, K., Sato, H., Obara, K., Ohtake, M., 2004. Configuration of subducting Philippine Sea plate beneath southwest Japan revealed from receiver function analysis based on the multivariate autoregressive model. J. Geophys. Res. 109, B04308. doi:10.1029/2003JB002774.

Soda, Y., Matsuzawa, T., Hasegawa, A., 2001. Seismic velocity structure of the crust and uppermost mantle beneath the northeastern Japan arc estimated from receiver functions. ZISIN2 54, 347–363 (in Japanese with English abstract).

The Headquarters for Earthquake Research Promotion, 2001. Long-term evaluation of the earthquake at Nankai Trough, http://www.jishin.go.jp/main/chousa/01sep_nankai/index.htm (in Japanese).

Ueno, H., Hatakeyama, S., Aketagawa, T., Funasaki, J., Hamada, N., 2002. Improvement of hypocenter determination procedures in the Japan Meteorological Agency. Quart. J. Seismol. 65, 123–134 (in Japanese with English abstract).

Wessel, P., Smith, W.H.F., 1998. New, improved version of the generic mapping tools released. EOS Trans. AGU 79, 579.

Yoshii, T., Sasaki, Y., Tada, T., Okada, H., Asano, S., Muramatsu, I., Moriya, T., 1974. The third Kurayoshi explosion and the crustal structure in the western part of Japan. J. Phys. Earth 22, 109–121.

Yuan, X., Sobolev, S.V., Kind, R., Oncken, O., Bock, G., Asch, G., Schurr, B., Graeber, F., Rudloff, A., Hanka, W., Wylegalla, K., Tibi, R., Haberland, Ch., Rietbrock, A., Giese, P., Wigger, P., Röwer, P., Zandt, G., Beck, S., Wallace, T., Pardo, M., Comte, D., 2000. Subduction and collision processes in the Central Andes constrained by converted seismic phases. Nature 408, 958–961.

Zhao, D., Horiuchi, S., Hasegawa, A., 1992. Seismic velocity structure of the crust beneath the Japan islands. Tectonophysics 212, 289–301.

Zhao, D., Mishra, O.P., Sanda, R., 2002. Influence of fluids and magma on earthquakes: seismological evidence. Phys. Earth Planet. Inter. 132, 249–267.

Zhu, L., 2000. Crustal structure across the San Andreas Fault, southern California from teleseismic converted waves. Earth Planet. Sci. Lett. 179, 183–190.

Zhu, L., Kanamori, H., 2000. Moho depth variation in southern California from teleseismic receiver functions. J. Geophys. Res. 105 (B2), 2969–2980.

Zorin, Y.A., Mordvinova, V.V., Turutanov, E.Kh., Belichenko, B.G., Artemyev, A.A., Kosarev, G..L., Gao, S.S., 2002. Low seismic velocity layers in the earth's crust beneath eastern Siberia (Russia) and central Mongolia: receiver function data and their possible geological implication. Tectonophysics 359, 307–327.